Contents

Method

Relative humidity (RH)

Relative humidity is calculated from the 2-m dew-point temperature (*Td*) and air temperature (*Ta*) using the improved Magnus formula. *Ta* and *Td* are expressed in ℃. Vapor pressure (*e*) and saturation vapor pressure (e_s) in hectopascals (hPa) are calculated as:

$$e = 6.112 \times \exp\left(\frac{17.67 \times Td}{Td + 243.5}\right),$$

$$e_s = 6.112 \times \exp\left(\frac{17.67 \times Ta}{Ta + 243.5}\right),$$

RH (%) is then derived as:

$$RH = \frac{e}{e_s} \times 100.$$

Heat Index (HI)

Heat Index is computed following the NOAA algorithm [1]. Air temperature *Ta* (°F) and *RH* (%) are first used to compute a simplified estimate:

$$HI_{simple} = \frac{Ta + 61 + 1.2 \times (Ta - 68) + 0.094 \times RH}{2}.$$

When the average of air temperature and the simplified estimate exceeds 80°F, i.e., (Ta + HI_{simple})/2 > 80 °F, we apply the full Rothfusz regression:

$$HI = -42.379 + 2.04901523Ta + 10.14333127RH - 0.22475541TaRH - 0.00683783Ta^2 - 0.05481717RH^2 + 0.00122874Ta^2RH + 0.00085282TaRH^2 - 0.00000199Ta^2RH^2.$$

If RH < 13% and 80 ≤ Ta ≤ 112 °F, we subtract an adjustment *ADJ1* from HI:

$$ADJ1 = \frac{13 - RH}{4} \times \sqrt{\frac{17 - |Ta - 95|}{17}}.$$

If RH > 85% and 80 ≤ Ta ≤ 87 °F, we add adjustment *ADJ2* to HI:

$$ADJ2 = \frac{RH - 85}{10} \times \frac{87 - Ta}{5}.$$

Hourly HI values are converted back to ℃, and the daily maximum HI is used for exposure analyses.

Wet-Bulb Globe Temperature (WBGT)

Wet-Bulb Globe Temperature integrates the effects of air temperature, humidity, radiation, and wind, and is widely used in occupational heat stress guidance [2]. WBGT is defined as:

$$WBGT = 0.7 \times T_{nwb} + 0.2 \times T_g + 0.1 \times Ta,$$

where T_{nwb} is the natural wet-bulb temperature and T_g is the black-globe temperature. Because direct calculation of T_{nwb} and T_g requires variables not available consistently across our data sources, we estimated WBGT using the proxy method described by Carter et al. [3]. This

formulation was selected because it is compatible with the available ERA5-Land inputs and has an observationally evaluated basis, although independent validation for Mediterranean conditions remains needed.

Black-globe temperature (T_g) is estimated from downward shortwave radiation $K_{\downarrow}$ (W m^{-2}), air temperature Ta (℃), and RH (%) as [3]:

$$T_g = 0.009624 \times K_{\downarrow} + 1.102 \times Ta - 0.00404 \times RH - 2.2776.$$

Natural wet-bulb temperature (T_{nwb}) is derived from the psychrometric wet-bulb temperature T_{pwb} using the approach implemented in Kestrel heat-stress monitors [3, 4], which incorporates wind speed (WS, m s^{-1}) and $K_{\downarrow}$. The psychrometric wet-bulb temperature is computed as [3, 4]:

$$T_{pwb} = 0.376 + 5.79e_a + (0.388 - 0.0465e_a)Ta,$$

where ambient vapor pressure e_a (kPa) is:

$$e_a = (\frac{RH}{100}) \times 0.6107 \times \exp(\frac{17.27\,Ta}{Ta+237.3}).$$

Subsequently, T_{nwb} is computed based on the difference between T_g and Ta.

When $T_g - Ta < 4$:

$$T_{nwb} = Ta - C \times (Ta - T_{pwb}),$$

with

$$C = \begin{cases} 0.85, & WS < 0.03\ ms^{-1} \\ 0.96 + 0.069log_{10}WS, & 0.03 \le WS \le 3.0\ ms^{-1} \\ 1.0, & WS > 3.0\ ms^{-1} \end{cases}$$

When $T_g - Ta \ge 4$:

$$T_{nwb} = T_{pwb} + 0.25 \times \left(T_g - Ta\right) + e,$$

with

$$e = \begin{cases} 1.1, & WS < 0.1\ ms^{-1} \\ \frac{0.1}{WS^{1.1}} - 0.2, & 0.1 \le WS \le 1.0\ ms^{-1} \\ -0.1, & WS > 1.0\ ms^{-1} \end{cases}$$

WBGT is computed at the hourly scale, and the daily maximum WBGT is used for exposure analyses.

Tables S1-S5

Table S1. Summary of literature comparing various heat stress indicators.

Year [Ref]	Regions	Indicators	Threshold	Key findings
2025 [5]	U.S.	Ta, HI	Absolute and Relative (95^{th})	1. Compared to HI, Ta severely underestimates the actual health risks in humid regions. 2. Exposure changes are extremely dramatic under absolute thresholds, but relatively moderate under relative thresholds.
2025 [6]	Global	Tw, HI, Humidex, WBGT, UTCI	Absolute and Relative (95^{th})	1. Metrics can disagree on the spatial pattern, and sometimes even the sign of heat-stress change, leading to large differences in population exposure. 2. Cross-metric spread is comparable to reanalysis/CMIP6 uncertainty and is driven mainly by different temperature–humidity weighting.
2025 [7]	North America	HI, Tw, WBGT, Humidex	Absolute	1. Irrigation significantly reduces daytime heat stress, with the strongest cooling/moistening effects and greatest HI reduction in arid zone. 2. ΔTw and ΔWBGT often oppose each other, and nocturnal Humidex/WBGT may increase, indicating elevated humid heat risk.
2024 [8]	Africa	HI, UTCI	Absolute	1. UTCI is more sensitive in areas characterized by high solar radiation and low humidity. 2. HI and UTCI disagree on the extent and seasonality of high-risk classes, so indicator choice shifts hotspot footprints.
2023 [9]	Not region-specific (sensitivity analysis)	Tw, AT, HI, UTCI, WBGT, sWBGT, Humidex	Not threshold-based (index sensitivity comparison)	1. Different indices weight temperature and humidity very differently. 2. At lower temperatures, AT/HI/UTCI are mainly temperature-driven, whereas Tw remains humidity-sensitive. 3. Same moisture-related change (e.g., irrigation) can yield opposite “heat-stress” responses depending on the index
2022 [10]	Europe	LST, Ta, RH, HI, Humidex	Not threshold-based	1. Lower urban RH partly compensates higher Ta, so daytime urban–rural heat stress (HI) differences are small. 2. LST is weakly related to Ta/HI and is a poor proxy for intra-urban heat-stress hotspots.
2022 [11]	Global	HI, Tw, WBGT	Absolute	1. HI produces higher values and more frequent events in dry-hot regions (e.g., North Africa). 2. Tw and WBGT are more critical for identifying deadly heat stress in humid regions (e.g., West Africa).
2022 [12]	Florida, US	HI, WBGT	Absolute	1. Coastal increases in HI/WBGT outpaced those in inland urban areas. 2. Urbanization played a minimal role compared to the influence of warming coastal waters.

2021 [13]	Global	HI, WBGT	Absolute	1. HI better captures the amplitude of extreme dry-heat events (e.g., Aleppo), while derived WBGT saturates at high temperatures and is more conservative in arid regions. 2. Total urban warming increased global exposure 52% more than population growth alone, with driving forces spatially heterogeneous (e.g., population-driven in West Asia vs warming-driven in the Nile Delta).
2021 [14]	Shanghai, China	Ta, WBGT, AppT	Relative (90^{th}, 95^{th}, 97.5^{th})	Ta amplifies heat islands all day, WBGT exacerbates daytime stress, while AppT most severely impacts nighttime comfort, particularly in less-urbanized districts.
2020 [15]	Yangtze River Delta urban agglomeration, China	LST, Ta, UTCI, Td, Tmrt	Absolute	1. LST shows the highest UHI intensity with strong spatial heterogeneity. 2. UTCI diverges significantly from Ta in urban/coastal areas, highlighting sensitivity to humidity and radiation.
2019 [16]	South Asian cities (Delhi, Dhaka, Faisalabad)	Ta, HI, WBGT, UTCI	Absolute	1. HI remains high post-monsoon due to humidity, while Ta drops. 2. UTCI and WBGT, which account for radiation, reveal strong heat stress even when Ta is moderate, especially in humid Dhaka.
2016 [17]	Houston, Texas, US	Ta, HI	Relative (95^{th}: Ta), Absolute (HI)	1. Land-use change increased HI (~2°C) more than Ta (~0.75°C). 2. Future scenario caused around 4-fold increase in extreme heat days.
2015 [18]	U.S. and southern Canada	Ta, HI, sWBGT, Humidex, AT, DI	Relative (95^{th})	1. In arid Phoenix, HI and Humidex show lower heat stress than Ta alone, due to the mitigating effect of low atmospheric moisture. 2. Future urban heat stress for AT, HI, and Humidex is 0.5–1.0 °C higher than for temperature.

Abbreviations: air temperature (Ta), wet-bulb temperature (Tw), mean radiant temperature (T_{mrt}), apparent temperature (AT), heat index (HI), wet-bulb globe temperature (WBGT), simplified wet-bulb globe temperature (sWBGT), human-perceived temperature (AppT), discomfort index (DI), Universal Thermal Climate Index (UTCI).

Table S2. Spatial agreement in exposure duration classification across metric pairs under absolute thresholds. Values show the percentage of evaluated pixels (%) classified into each of the nine joint low/medium/high (L/M/H) classes for the six pairwise combinations. The evaluated pixel set is defined as pixels where both metrics are available and at least one metric has positive exposure duration (>0). Diagonal cells (L&L, M&M, H&H) indicate agreement, whereas off-diagonal cells indicate classification shifts between metrics. The final column ("Mean") reports the mean percentage across the six metric pairs for each joint class.

Group	LST vs. Ta	LST vs. HI	LST vs. WBGT	Ta vs. HI	Ta vs. WBGT	HI vs. WBGT	Mean
L & L	30.5	33.1	32.4	33.1	32.5	33.3	32.5
L & M	8.9	0.3	1.4	0.3	0.8	27.4	6.5
L & H	1.7	0.0	0.2	0.0	0.0	19.0	3.5
M & L	3.2	31.6	26.4	31.7	27.7	0.2	20.1
M & M	22.1	1.7	6.1	1.5	5.3	5.8	7.1
M & H	4.2	0.1	0.5	0.1	0.3	4.2	1.6
H & L	0.2	27.8	16.8	28.4	17.7	0.0	15.2
H & M	2.1	1.8	4.7	1.6	4.9	0.1	2.5
H & H	27.2	3.7	11.5	3.3	10.7	10.1	11.1

Table S3. Joint top-decile hotspot shares and country contributions under absolute thresholds. The first row reports the percentage of evaluated pixels (%) jointly falling in the top decile (90–100%) for both metrics. The remaining rows list the top contributing countries; percentages denote each country's share of all top–top pixels across the study region (country top–top pixel count divided by the regional total).

Group	LST vs. Ta	LST vs. HI	LST vs. WBGT	Ta vs. HI	Ta vs. WBGT	HI vs. WBGT
Top–top (90–100%)	8.0	1.1	3.3	1.0	3.2	3.0
Top contributing countries (share of regional top–top pixels)						
1	Algeria (14.8%)	Tunisia (19.7%)	Egypt (27.9%)	Tunisia (19.5%)	Egypt (32.2%)	Tunisia (19.5%)
2	Egypt (14.5%)	Algeria (16.6%)	Algeria (14.4%)	Egypt (16.2%)	Algeria (13.5%)	Algeria (18.0%)
3	Turkey (12.0%)	Morocco (15.4%)	Morocco (14.3%)	Algeria (16.1%)	Morocco (13.2%)	Egypt (15.9%)

Table S4. Spatial agreement in exposure duration classification across metric pairs under relative thresholds. Values show the percentage of evaluated pixels (%) classified into each of the nine joint low/medium/high (L/M/H) classes for the six pairwise combinations. Diagonal cells (L&L, M&M, H&H) indicate agreement, while off-diagonal cells reveal classification shifts between metrics. The final column ("Mean") reports the mean percentage across the six metric pairs for each joint class.

Group	LST vs. Ta	LST vs. HI	LST vs. WBGT	Ta vs. HI	Ta vs. WBGT	HI vs. WBGT	Mean
L & L	30.9	30.3	30.0	31.4	30.9	32.4	31.0
L & M	3.6	4.1	4.3	2.3	2.8	1.3	3.0
L & H	0.4	0.6	0.6	0.1	0.2	0.1	0.3
M & L	2.7	4.3	4.5	3.3	3.8	1.3	3.3
M & M	26.9	24.6	24.2	27.4	26.3	30.5	26.7
M & H	3.0	3.6	3.9	2.4	3.0	1.3	2.9
H & L	0.1	1.2	1.2	1.1	1.1	0.1	0.8
H & M	2.6	3.4	3.7	2.5	3.0	1.3	2.8
H & H	29.8	28.0	27.7	29.6	29.0	31.8	29.3

Table S5. Joint top-decile hotspot shares and country contributions under relative thresholds. The first row reports the percentage of evaluated pixels (%) jointly falling in the top decile (90–100%) for both metrics. The remaining rows list the top contributing countries; percentages denote each country's share of all top–top pixels across the study region (country top–top pixel count divided by the regional total).

Group	LST vs. Ta	LST vs. HI	LST vs. WBGT	Ta vs. HI	Ta vs. WBGT	HI vs. WBGT
Top–top (90–100%)	8.5	7.8	7.7	8.4	8.1	9.4
Top contributing countries (share of regional top–top pixels)						
1	France (23.8%)	France (23.7%)	France (22.9%)	France (23.9%)	France (22.7%)	France (20.6%)
2	Italy (18.6%)	Italy (18.4%)	Italy (18.4%)	Italy (18.0%)	Italy (18.3%)	Italy (17.7%)
3	Spain (10.3%)	Spain (10.7%)	Spain (10.9%)	Spain (11.4%)	Spain (11.8%)	Spain (11.4%)

Figures S1-18

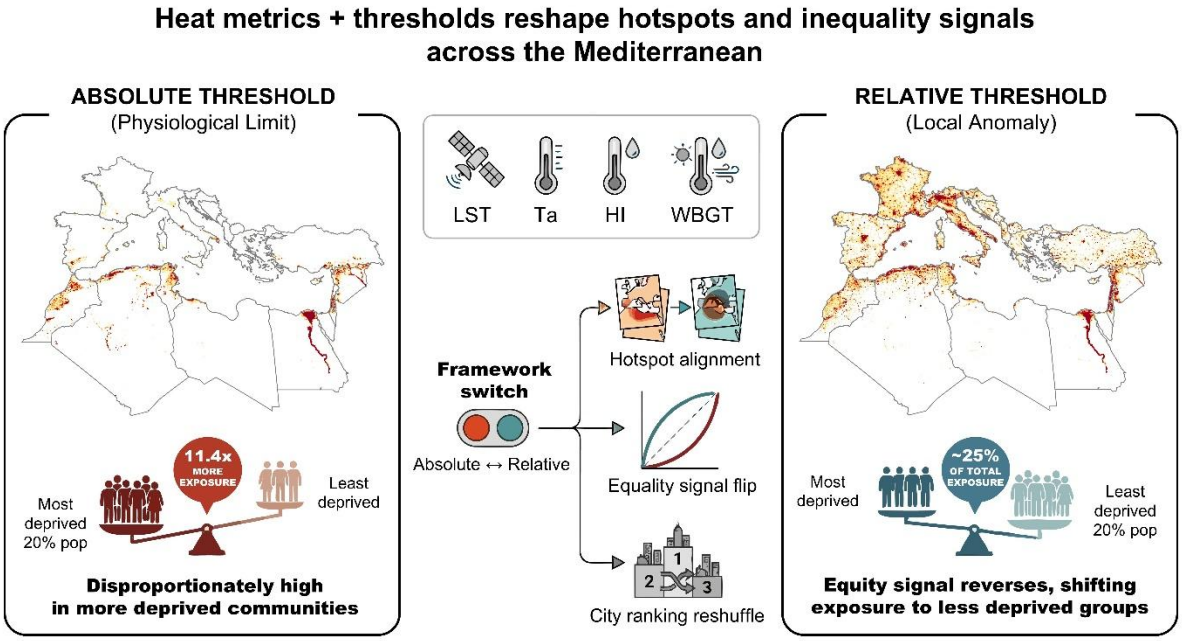

Fig. S1. Schematic overview of the study framework and main findings. The figure summarizes how comparing four heat metrics (LST, Ta, HI, and WBGT) under absolute versus relative thresholds changes hotspot alignment, exposure–deprivation patterns, and city-level rankings across the Mediterranean.

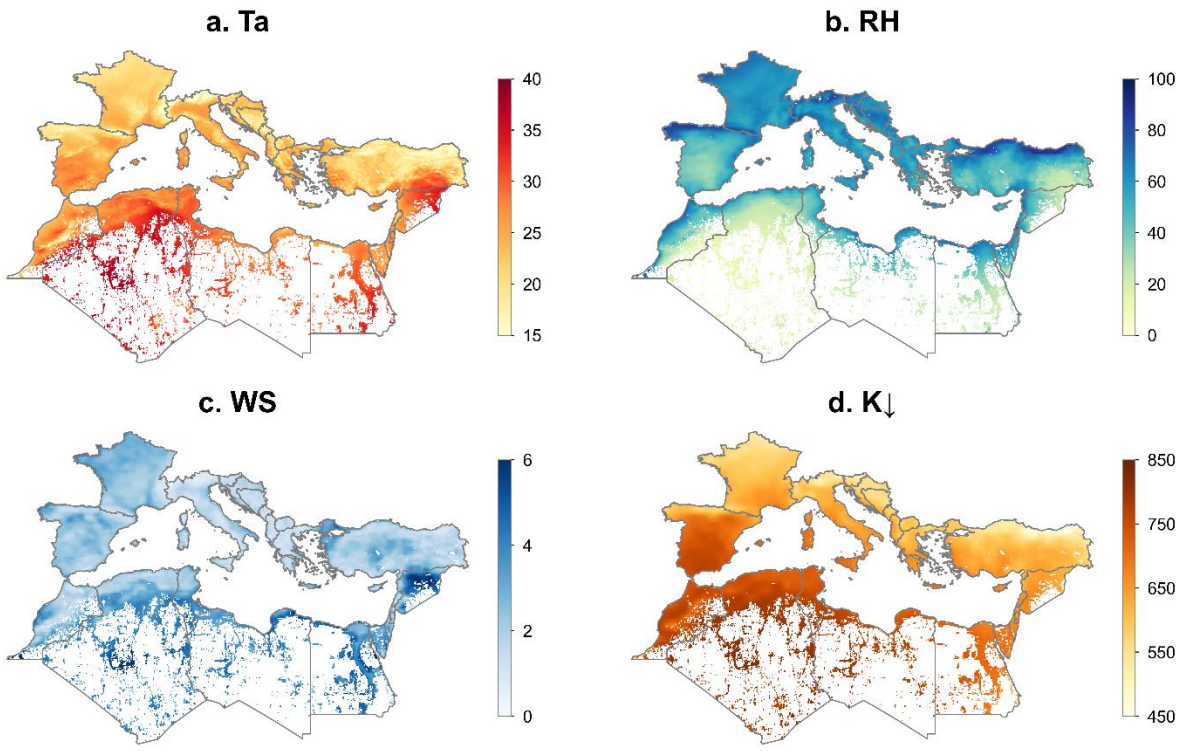

Fig. S2. Summer-mean meteorological fields across the study domain. Summer averages of **(a)** daily-mean 2 m air temperature, **(b)** daily-mean relative humidity, **(c)** daily-mean 10 m wind speed, **(d)** daytime-mean downward shortwave radiation from ERA5-Land.

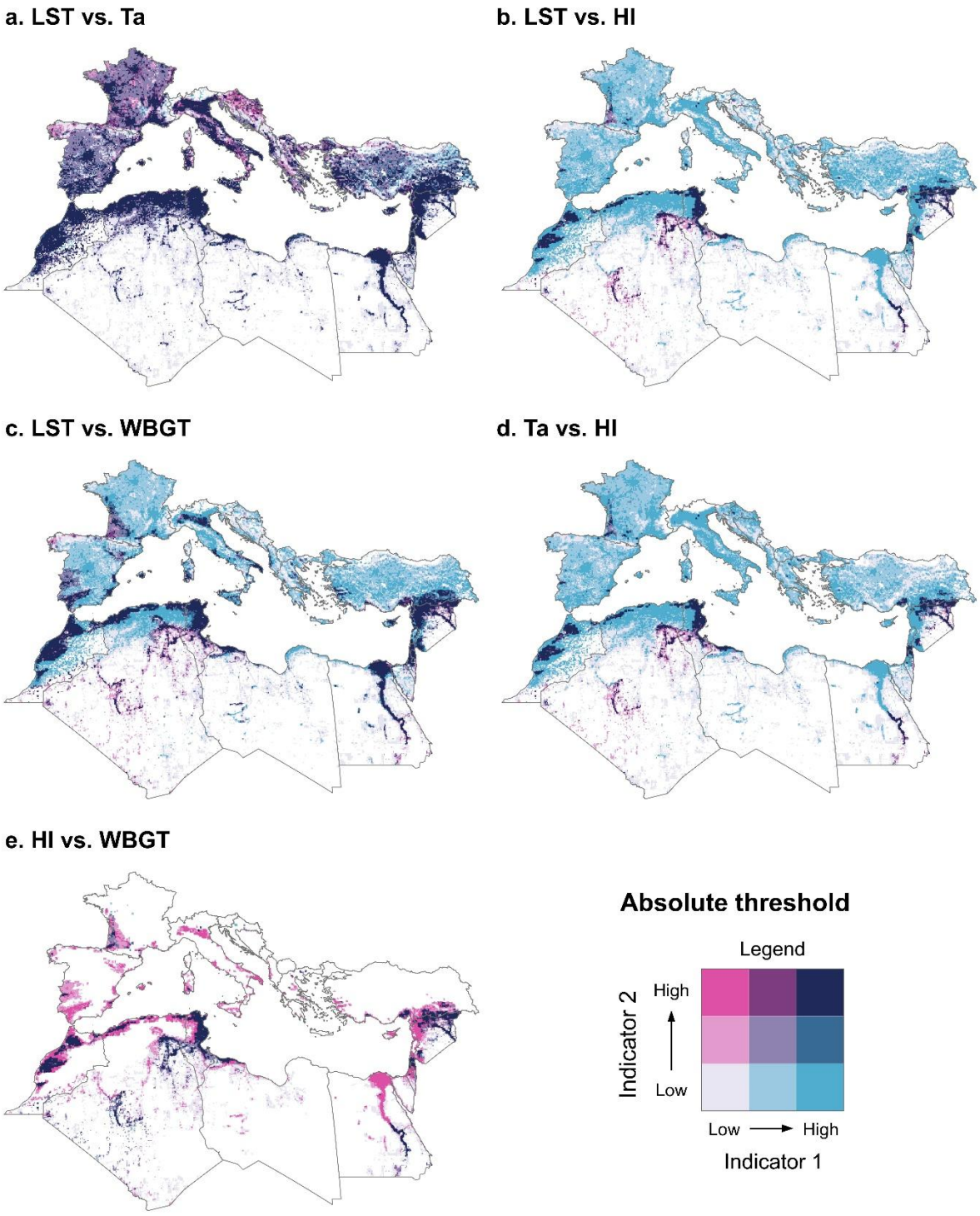

Fig. S3. Bivariate classification of exposure duration across metric pairs under absolute thresholds. Each map shows the joint tercile (low/medium/high) classification for **(a)** LST vs. Ta, **(b)** LST vs. HI, **(c)** LST vs. WBGT, **(d)** Ta vs. HI, and **(e)** HI vs. WBGT.

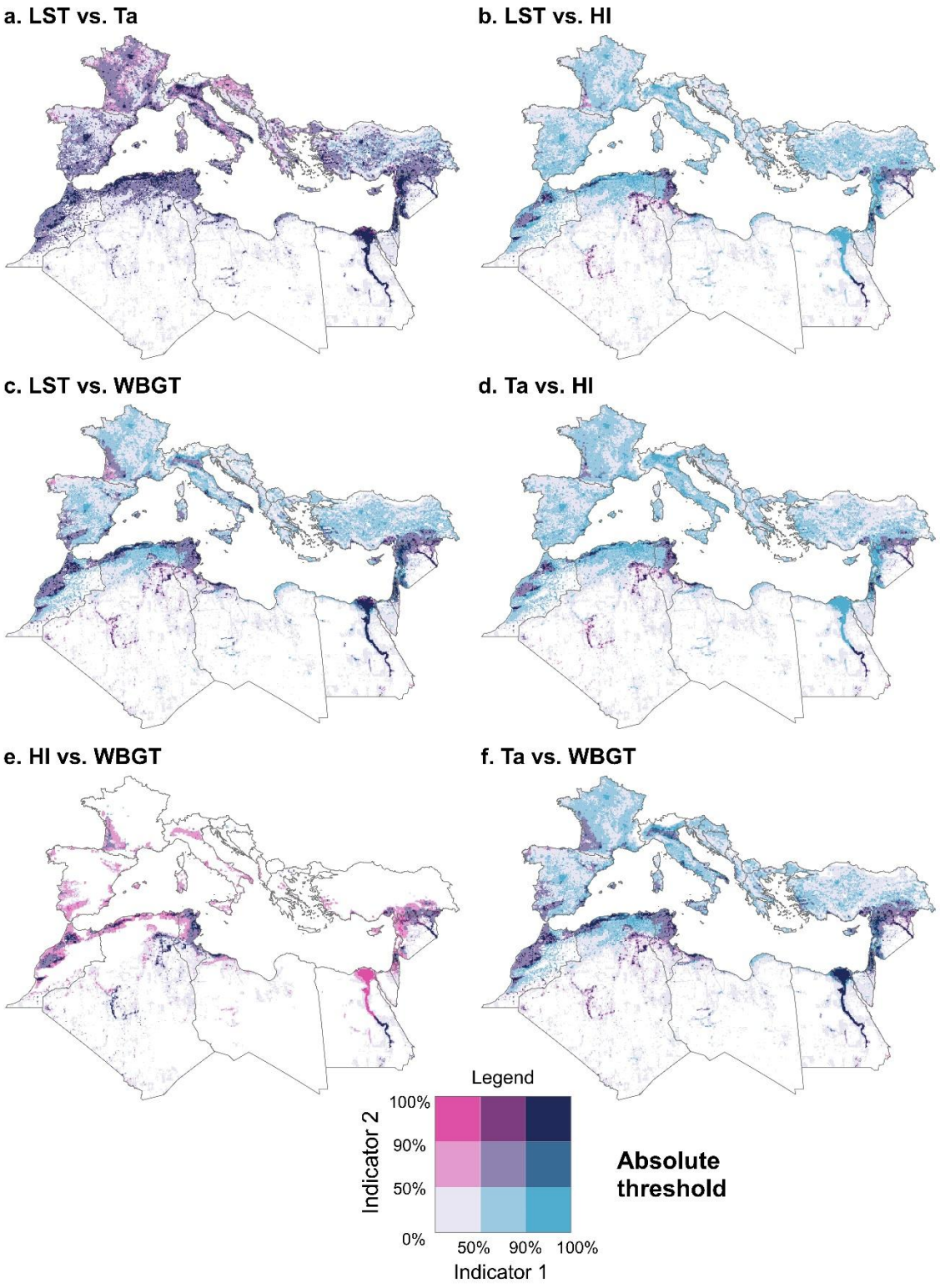

Fig. S4. Bivariate classification of exposure duration across metric pairs under absolute thresholds using asymmetric quantile bins. Each map shows the joint classification for **(a)** LST vs. Ta, **(b)** LST vs. HI, **(c)** LST vs. WBGT, **(d)** Ta vs. HI, and **(e)** HI vs. WBGT, and **(f)** Ta vs. WBGT, where values in each metric are grouped into three quantile classes: 0–50th, 50–90th, and 90–100th percentiles.

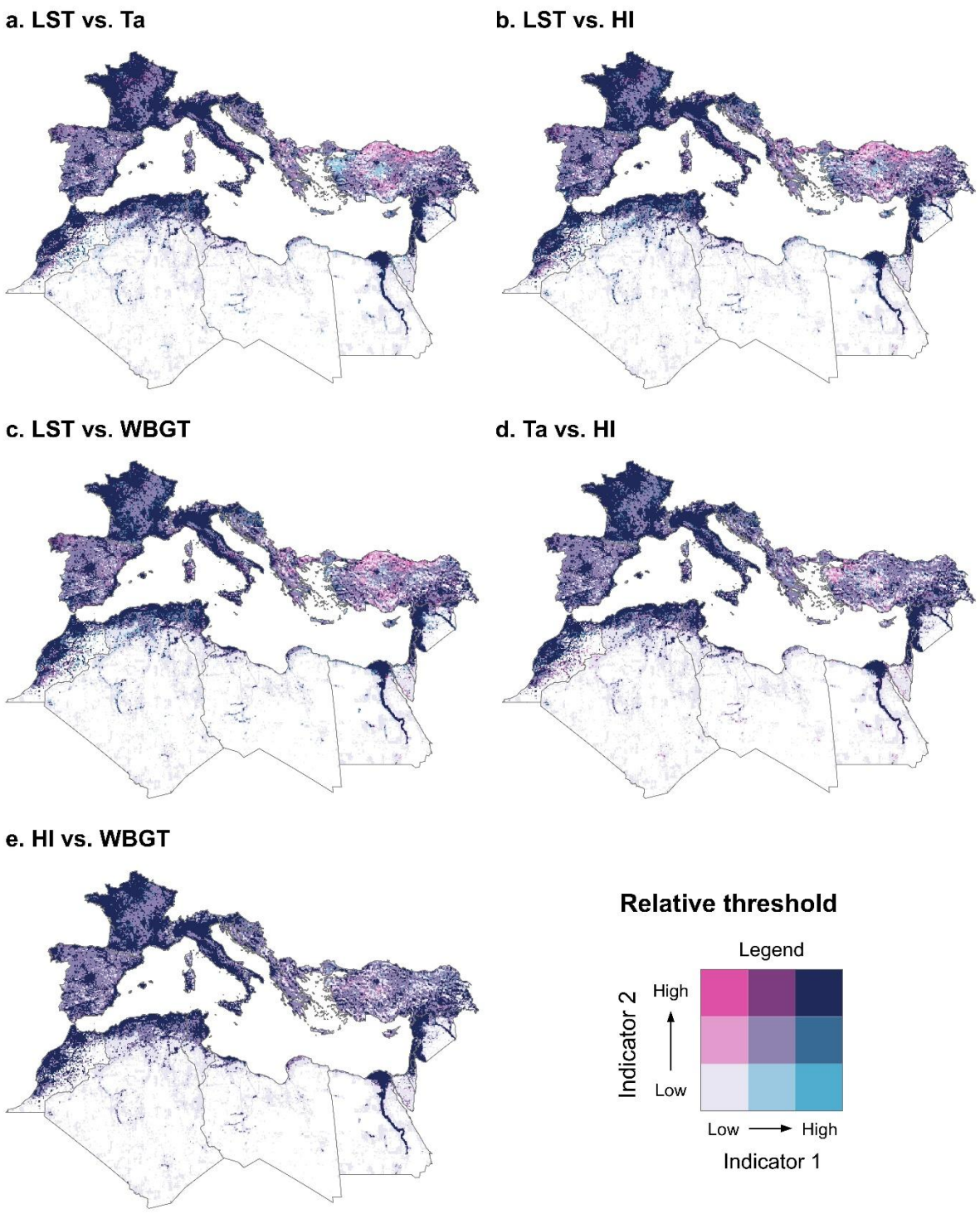

Fig. S5. Bivariate classification of exposure duration across metric pairs under relative thresholds. Each map shows the joint tercile (low/medium/high) classification for **(a)** LST vs. Ta, **(b)** LST vs. HI, **(c)** LST vs. WBGT, **(d)** Ta vs. HI, and **(e)** HI vs. WBGT.

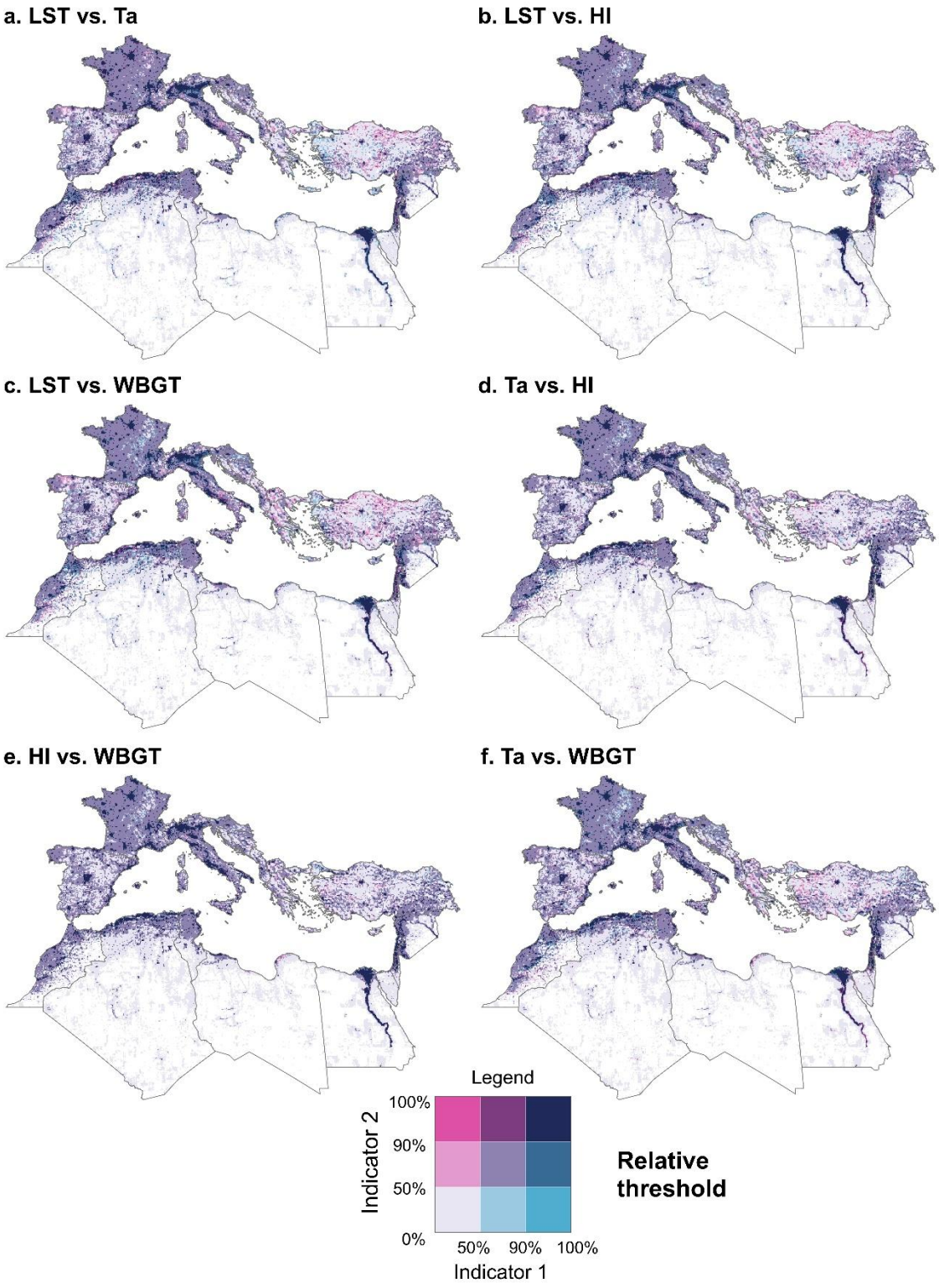

Fig. S6. Bivariate classification of exposure duration across metric pairs under relative thresholds using asymmetric quantile bins. Each map shows the joint classification for **(a)** LST vs. Ta, **(b)** LST vs. HI, **(c)** LST vs. WBGT, **(d)** Ta vs. HI, and **(e)** HI vs. WBGT, and **(f)** Ta vs. WBGT, where values in each metric are grouped into three quantile classes: 0–50th, 50–90th, and 90–100th percentiles.

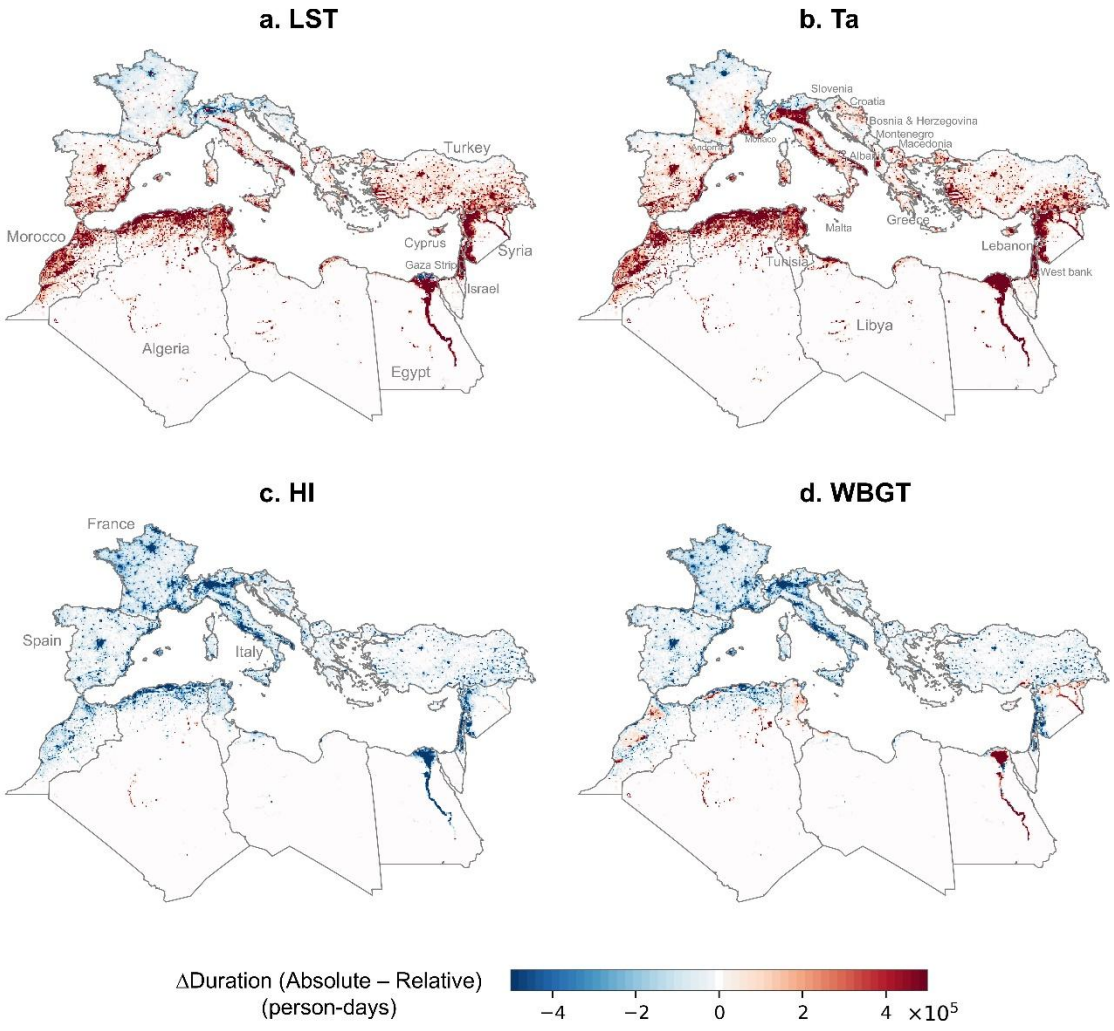

Fig. S7. Threshold-driven differences in exposure duration across heat metrics. Maps show ΔDuration = Duration(Absolute) − Duration(Relative) (person-days) for **(a)** LST, **(b)** Ta, **(c)** HI, and **(d)** WBGT. Red indicates higher exposure under the absolute threshold, whereas blue indicates higher exposure under the relative threshold.

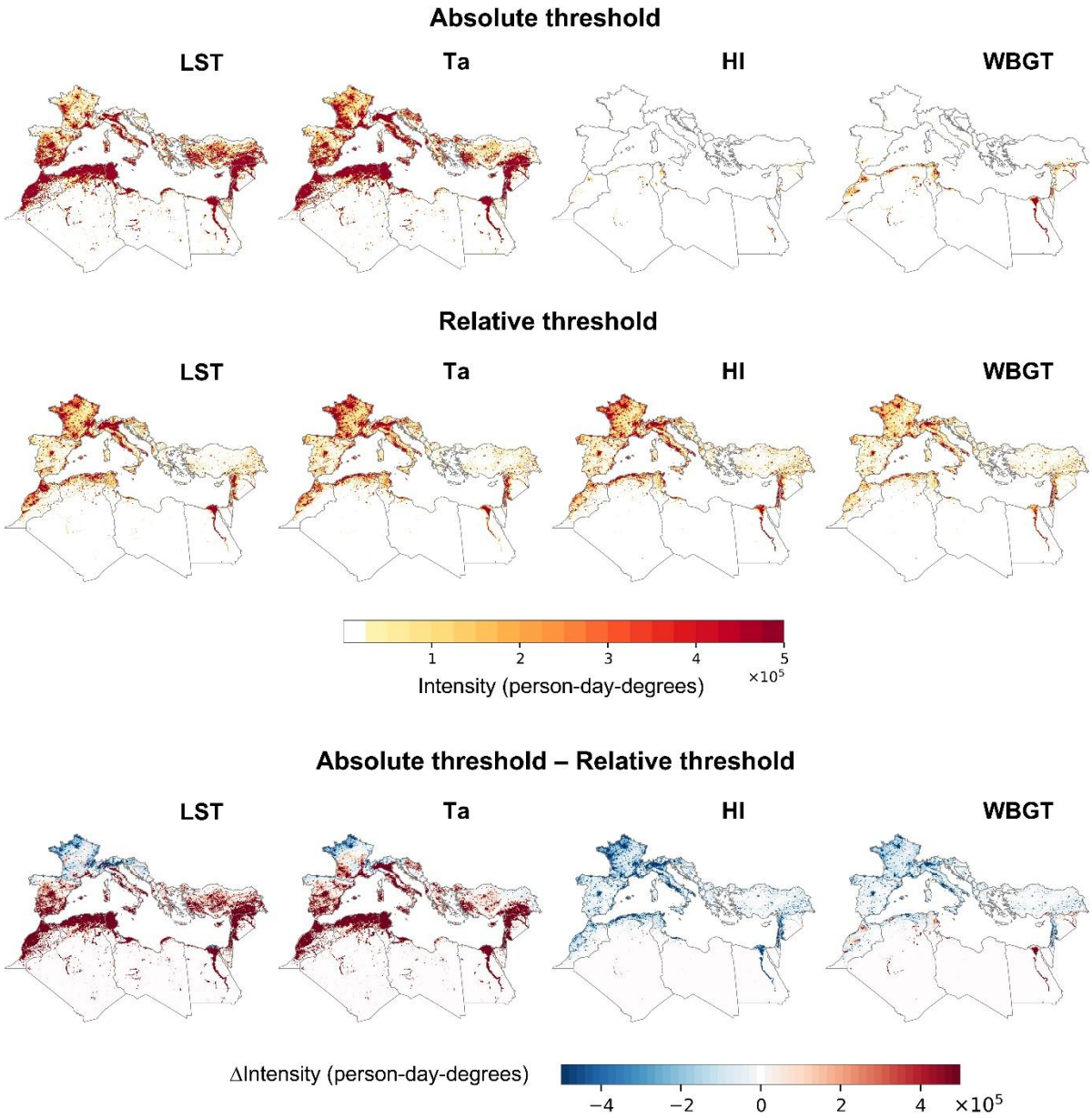

Fig. S8. Spatial distribution of exposure intensity across metrics and threshold frameworks. Maps show exposure intensity (person-day-degrees) for LST, Ta, HI, and WBGT under absolute thresholds (top row) and relative thresholds (middle row). The bottom row shows the difference in intensity, ΔIntensity = Intensity(Absolute) − Intensity(Relative). Red indicates higher intensity under the absolute threshold, whereas blue indicates higher intensity under the relative threshold. For visual clarity, outputs are aggregated to 10 km for display.

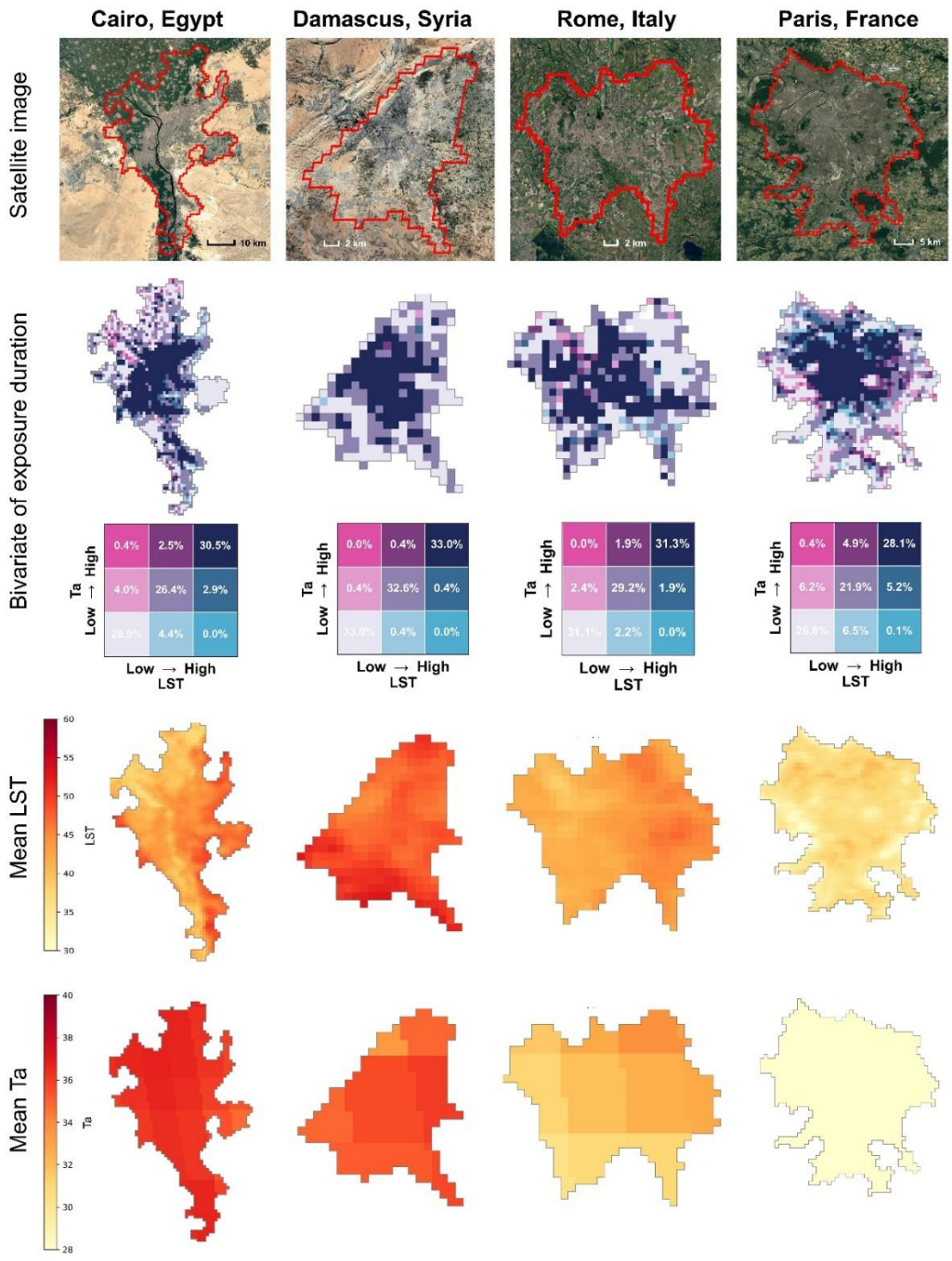

Fig. S9. City examples of bivariate exposure patterns under absolute thresholds and mean summer heat. Columns show Cairo (Egypt), Damascus (Syria), Rome (Italy), and Paris (France). Top row: satellite imagery with city boundaries. Second row: bivariate tercile map of exposure duration for LST (x-axis) and Ta (y-axis); terciles are computed within each city using evaluated pixels (with valid values and positive duration in at least one metric), to emphasize intra-urban contrasts. Inset 3×3 matrices give the percentage of evaluated pixels in each joint low/medium/high class. Bottom rows: mean summer daily maximum LST and Ta (°C). These high-exposure cities are selected to span distinct climatic settings across the study region, including hot-arid river-valley (Cairo), semi-arid inland (Damascus), Mediterranean coastal (Rome), and temperate urban (Paris).

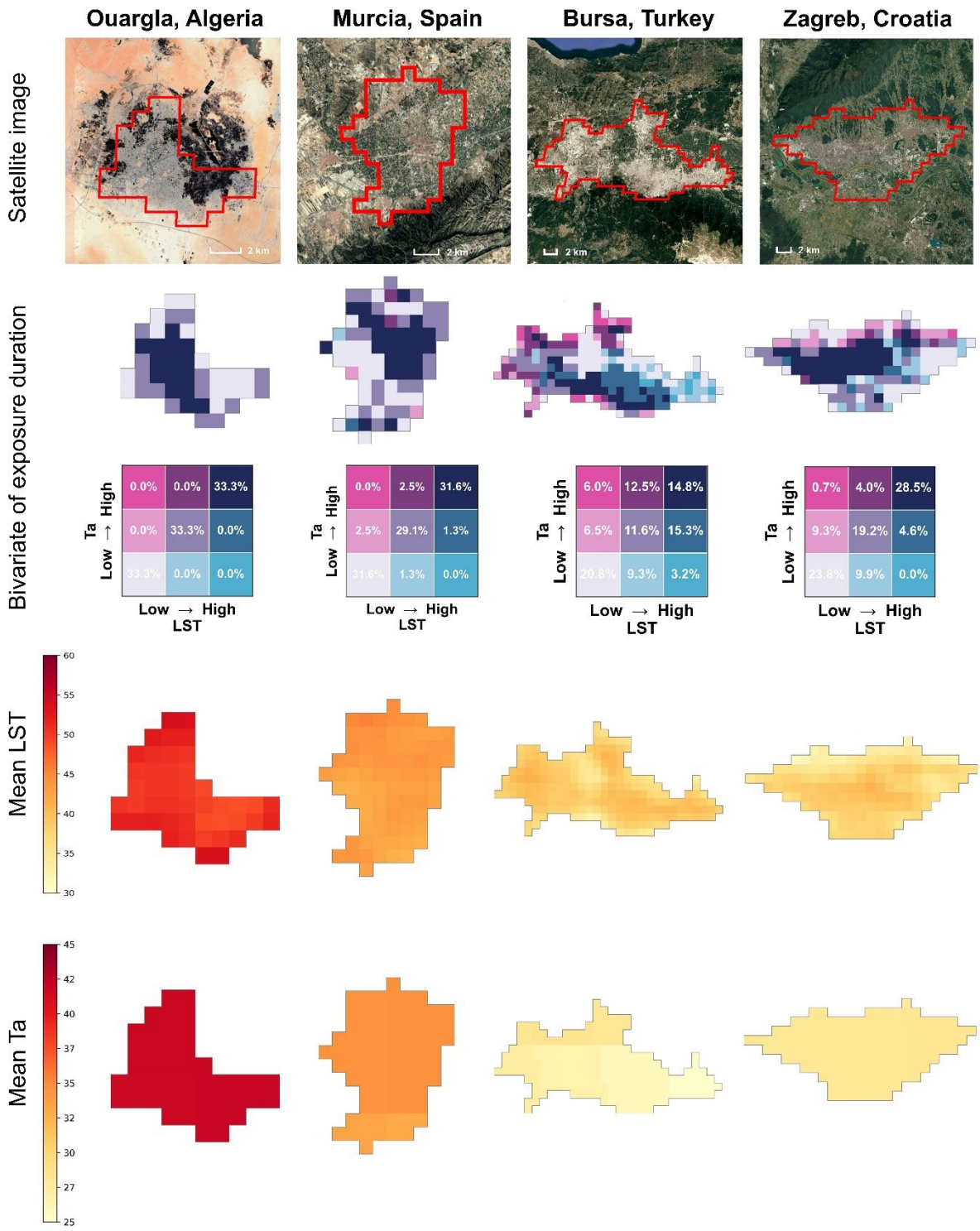

Fig. S10. Mid-ranked city examples for exposure duration under absolute thresholds, as in Fig. S9. Columns show Ouargla (Algeria), Murcia (Spain), Bursa (Turkey), and Zagreb (Croatia). Rows and bivariate tercile calculations follow **Fig. S9**. These mid-ranked cities are selected to span contrasting climatic and geographic contexts, including hot-arid Saharan (Ouargla), Mediterranean coastal plain (Murcia), near-coastal Marmara basin (Bursa), and temperate continental (Zagreb).

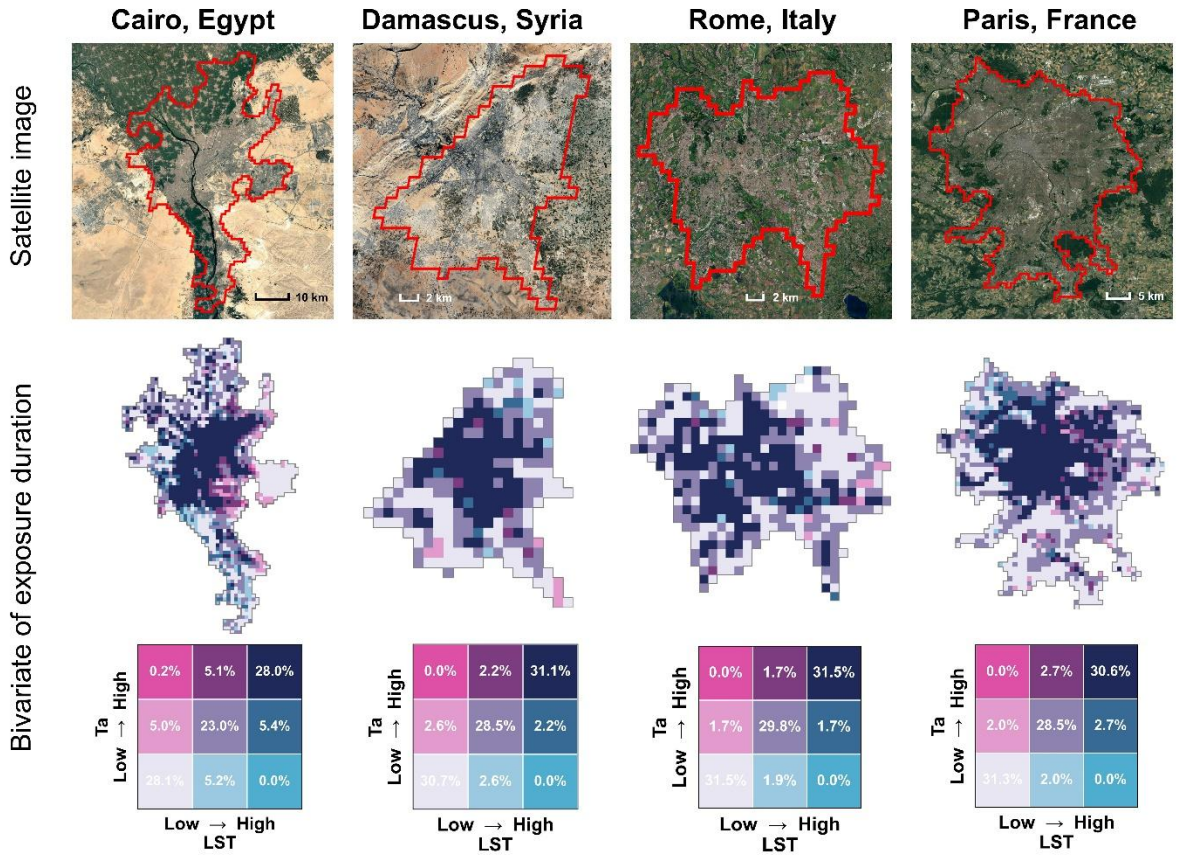

Fig. S11. As in Fig. S9, but using relative thresholds (same cities).

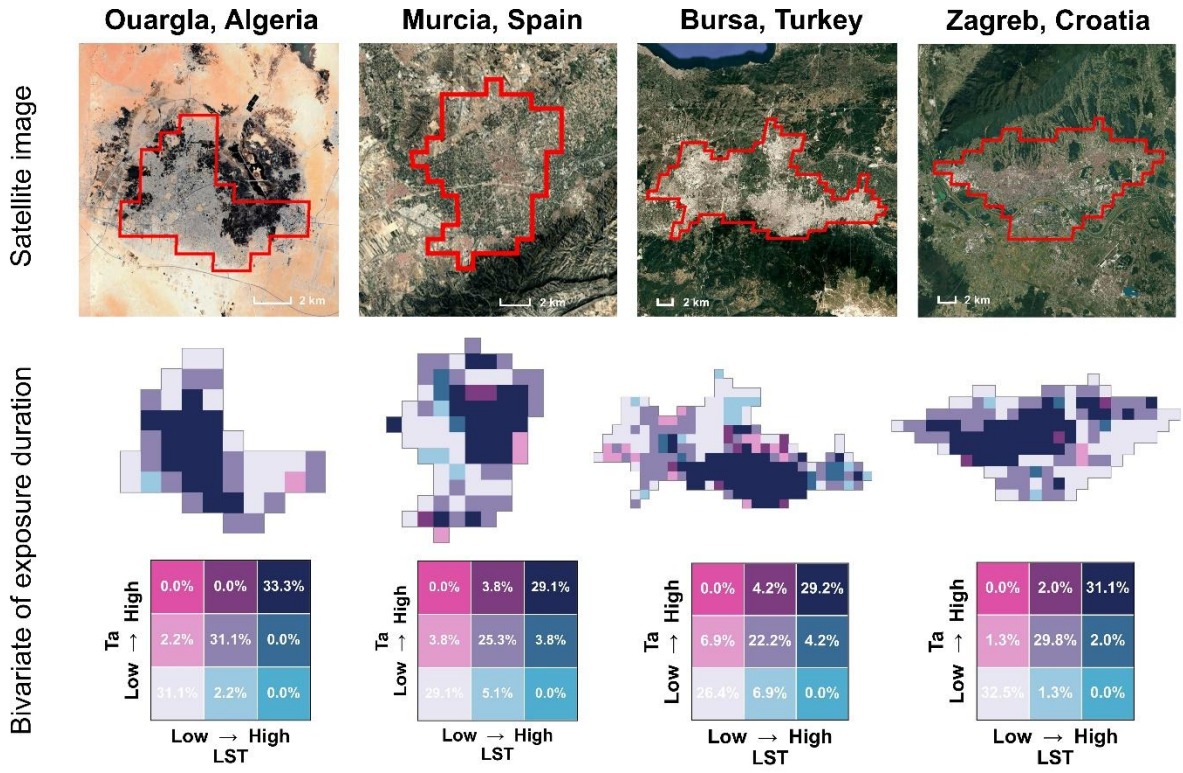

Fig. S12. As in Fig. S10, but using relative thresholds (same cities).

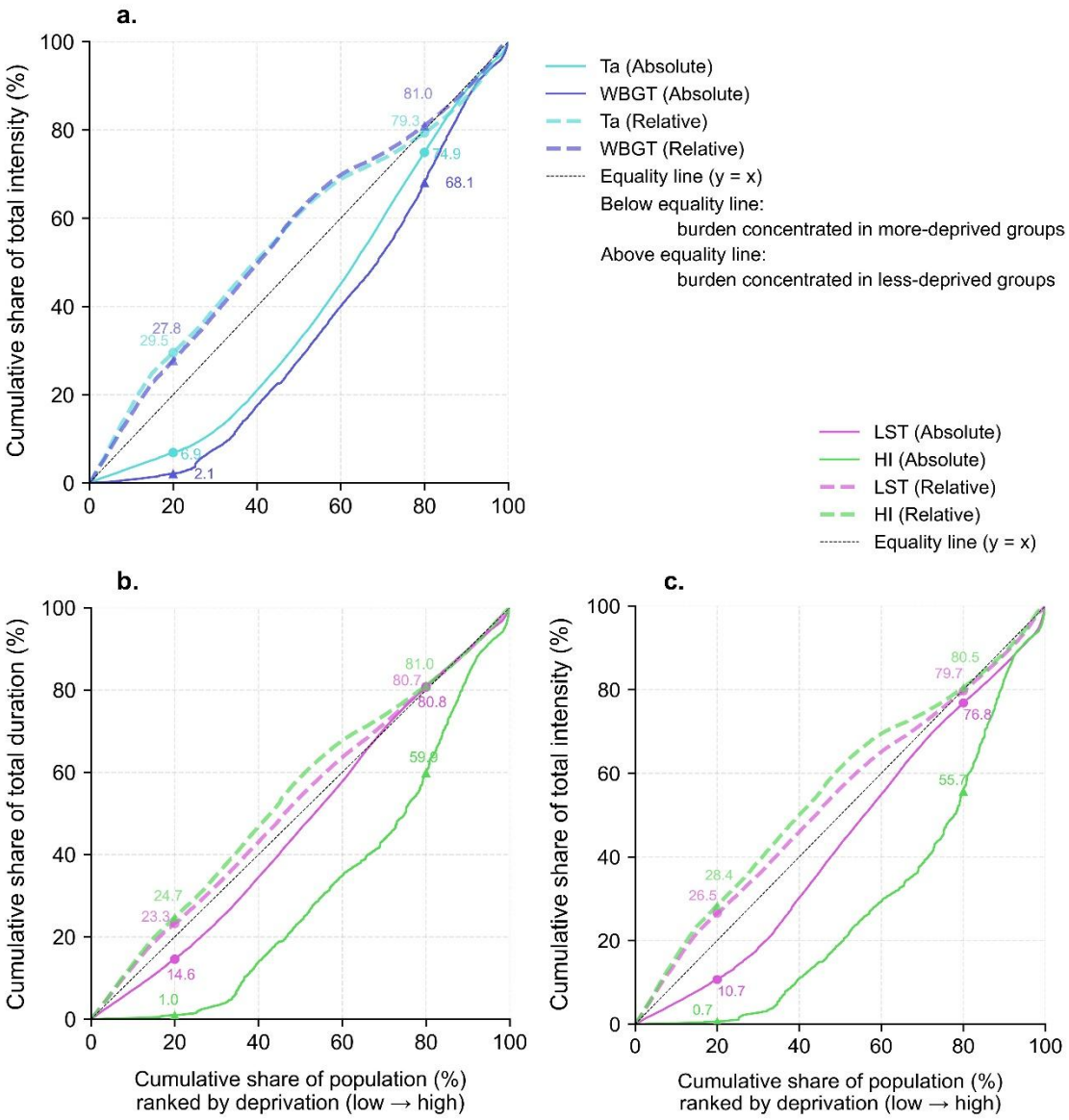

Fig. S13. Socioeconomic inequality in heat exposure across metrics and burden measures. (a) Deprivation-ranked cumulative share curves of intensity (person-day-degrees) for Ta and WBGT. **(b)** Deprivation-ranked cumulative share curves of duration (person-days) for LST and HI. **(c)** Deprivation-ranked cumulative share curves of intensity (person-day-degrees) for LST and HI. Populations are ordered from low to high deprivation. The 45° line denotes proportional burden; curves below (above) indicate that burden is disproportionately concentrated toward more (less) deprived populations.

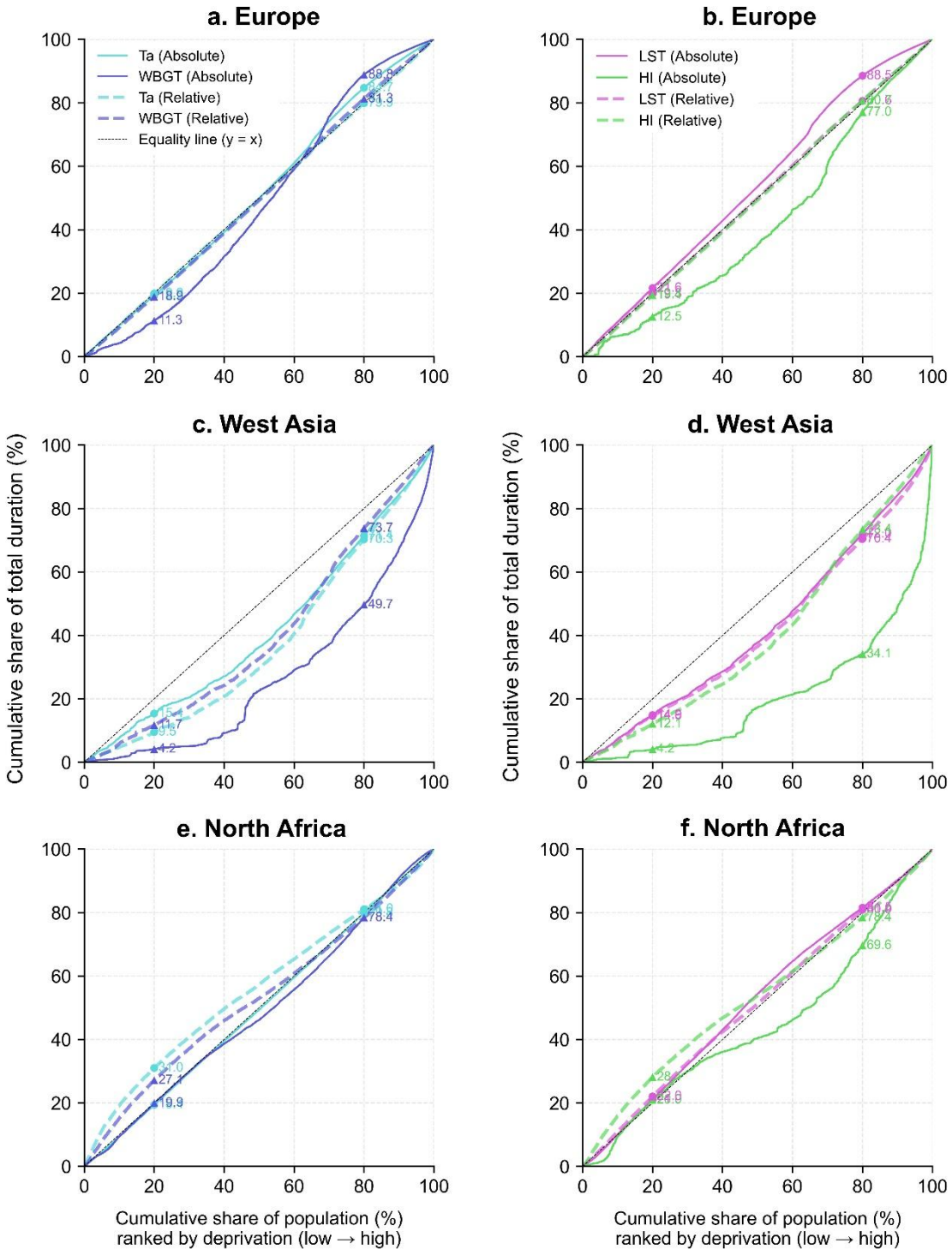

Fig. S14. Deprivation-ranked cumulative share curves of exposure duration across the region. Panels show Europe **(a–b)**, West Asia **(c–d)**, and North Africa **(e–f)**. In each region, Ta and WBGT are shown in **(a,c,e)** and LST and HI in **(b,d,f)**. Curves plot cumulative burden (y-axis; person-days) against cumulative population share (x-axis), with populations ordered from low to high deprivation. The 45° line denotes proportional burden; curves below (above) indicate disproportionate burden among more (less) deprived populations.

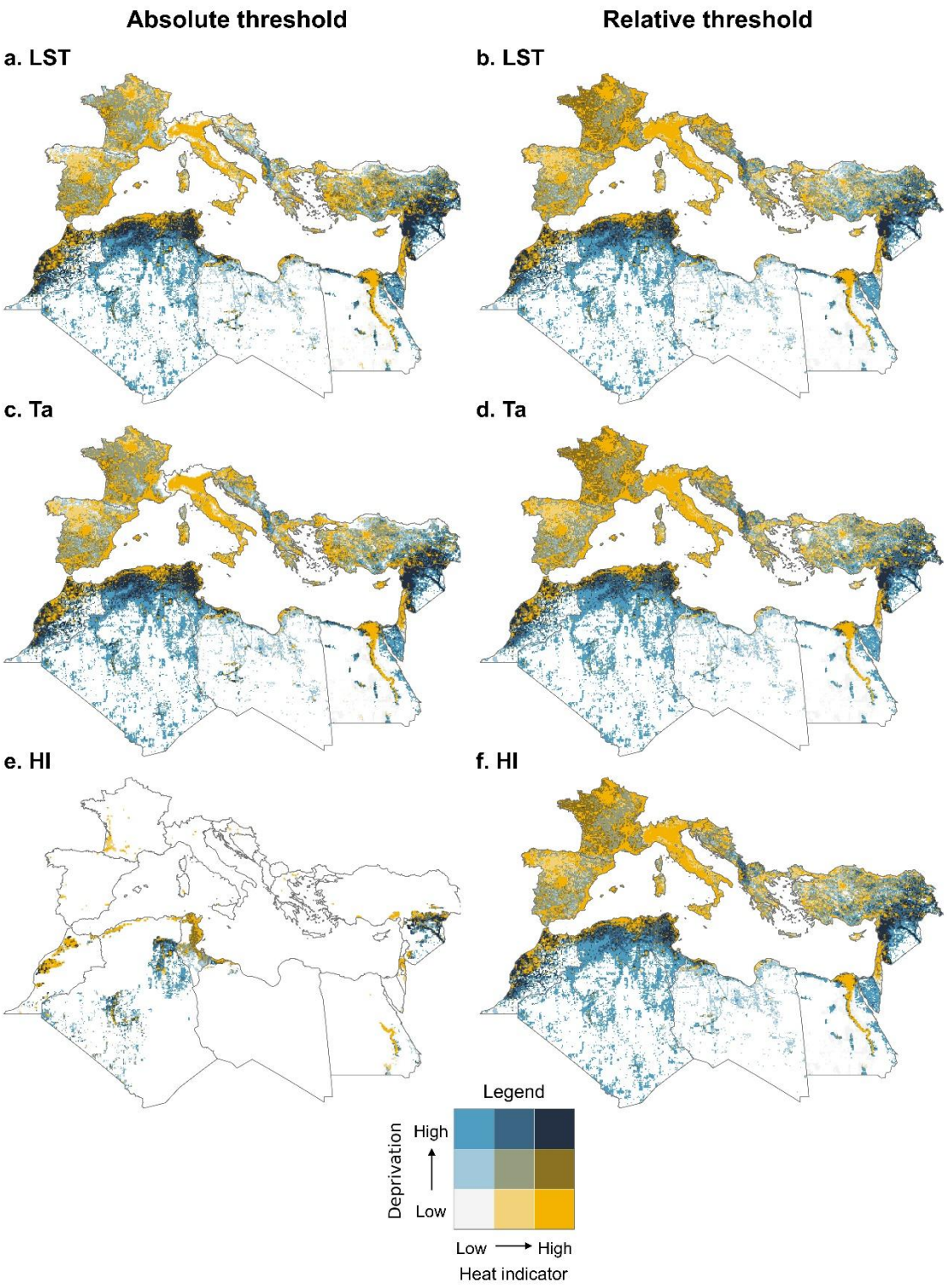

Fig. S15. Spatial co-occurrence of heat exposure and deprivation. Bivariate tercile maps of exposure duration and deprivation under **(a, c, e)** absolute and **(b, d, f)** relative thresholds. Heat indicators include **(a-b)** LST, **(c-d)** Ta, and **(e-f)** HI. Exposure duration and deprivation are each grouped into three equal-frequency terciles (low/medium/high) using pixels with positive exposure duration and valid GRDI; paired terciles yield nine joint classes.

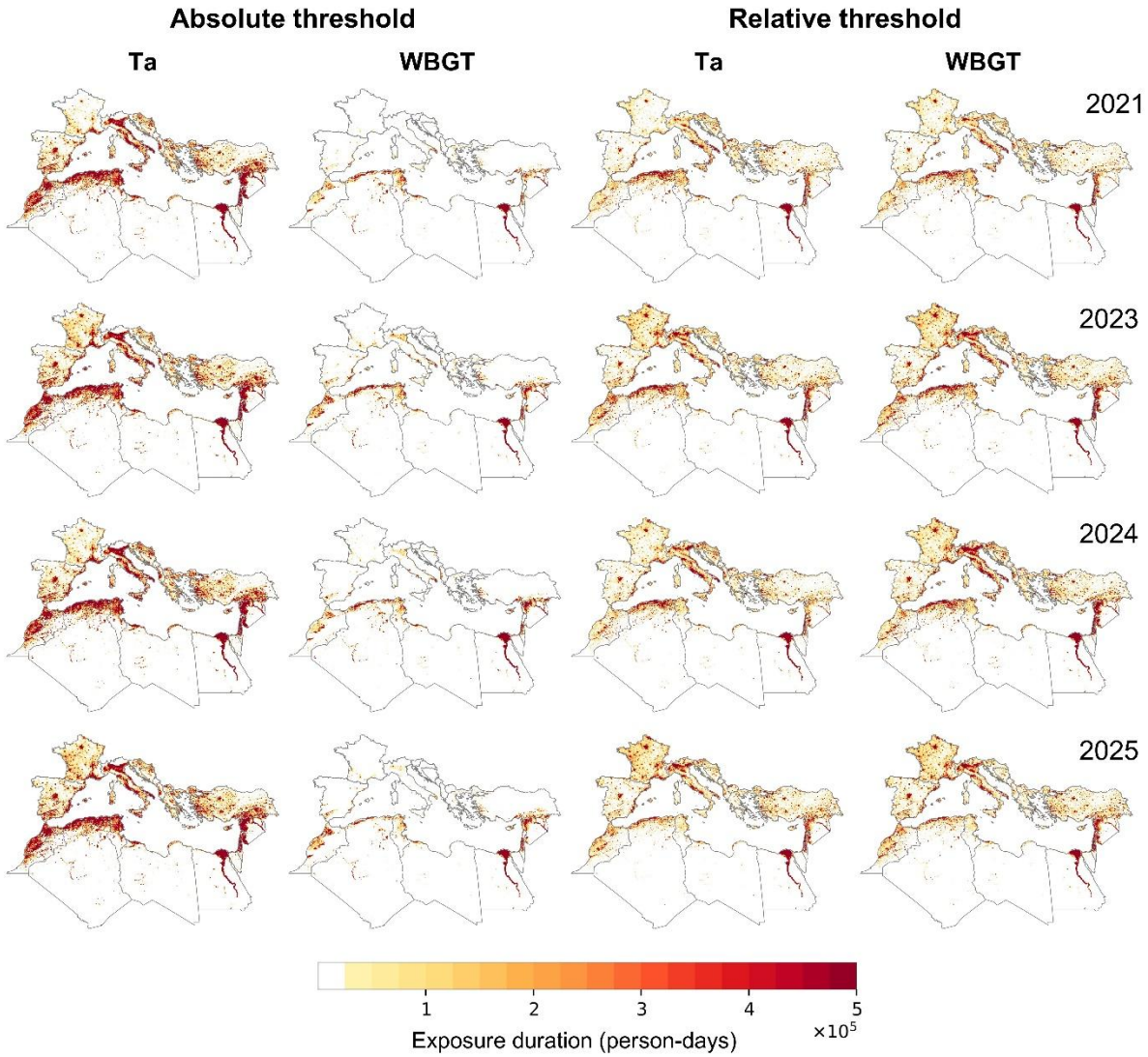

Fig. S16. Exposure duration (person-days) for Ta and WBGT under absolute and relative thresholds in 2021, 2023, 2024, and 2025. Maps are aggregated to 10 km for display. The same summer window and workflow as in **Section 2** were applied to each year (15 June–15 September).

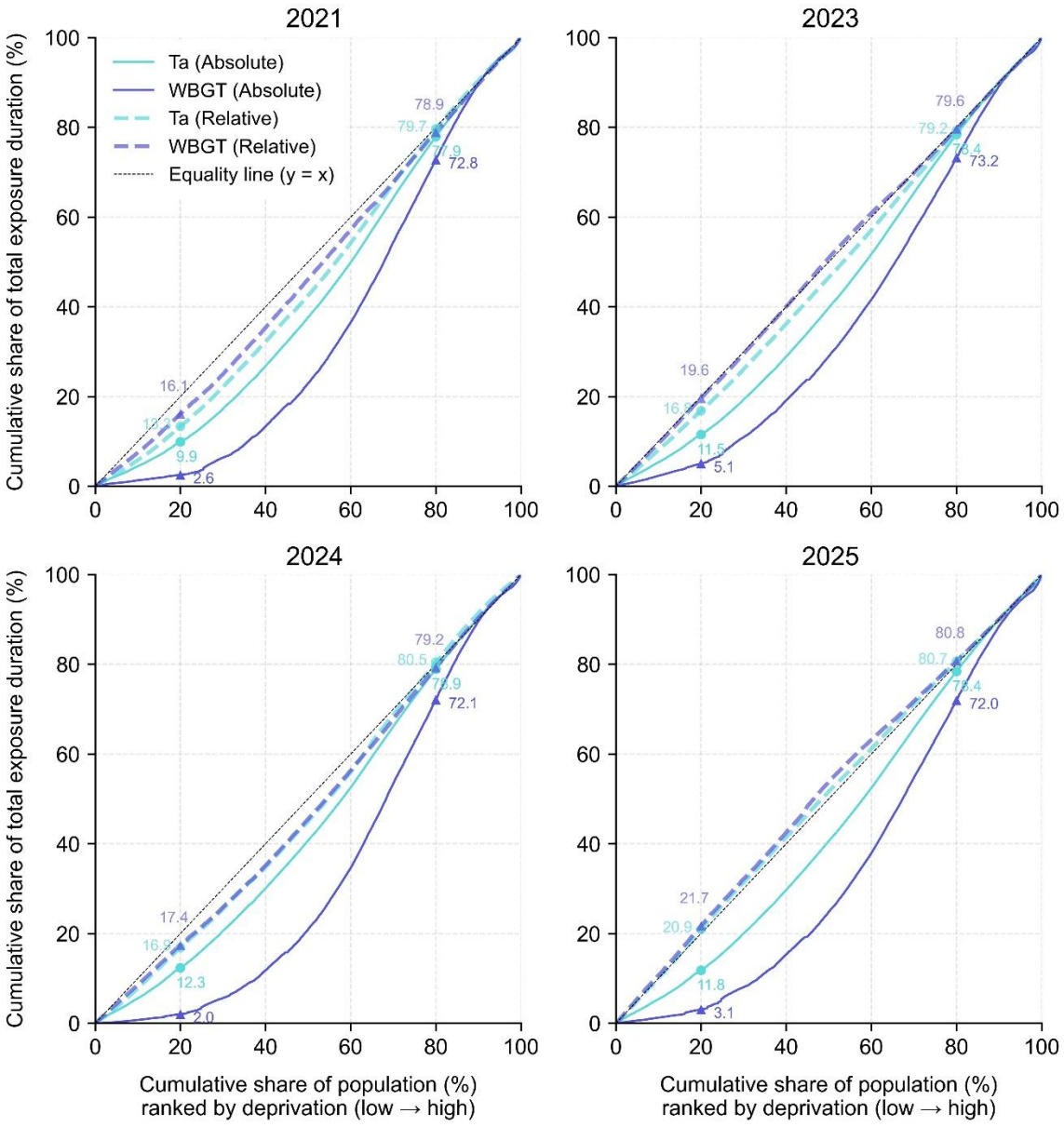

Fig. S17. Deprivation-ranked cumulative share curves for exposure duration (person-days) under absolute and relative thresholds in 2021, 2023, 2024, and 2025. Populations are ordered from low to high deprivation. The 45° line denotes proportional burden. Across years, absolute-threshold curves remain more concentrated toward deprived populations, whereas relative-threshold curves shift closer to proportionality.

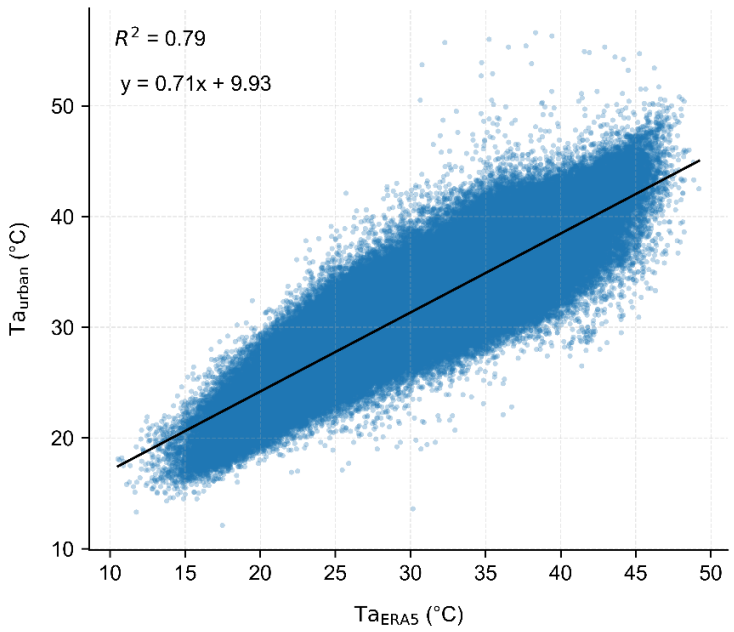

Fig. S18. Temperature correlation across urban settlement regions in the Mediterranean, summers 2012–2020. Scatter plot of daily maximum air temperature from ERA5-Land (Ta_{ERA5}) versus the 1-km urban air temperature product (T_{urban}; [19]) sampled over urban settlement pixels. Sample points were randomly selected within urban regions for each country (up to 100 points per country), enforcing a minimum 1-km separation between points. The solid line shows the least-squares linear regression; the fitted equation and R^2 are reported on the panel.

References

[1] NOAA, The Heat Index Equation, 1990. https://www.wpc.ncep.noaa.gov/html/heatindex_equation.shtml.
[2] J.C. Liljegren, R.A. Carhart, P. Lawday, S. Tschopp, R. Sharp, Modeling the wet bulb globe temperature using standard meteorological measurements, Journal of occupational and environmental hygiene 5(10) (2008) 645-655.
[3] A.W. Carter, B.F. Zaitchik, J.M. Gohlke, S. Wang, M.B. Richardson, Methods for estimating wet bulb globe temperature from remote and low-cost data: A comparative study in Central Alabama, GeoHealth 4(5) (2020) e2019GH000231.
[4] T.E. Bernard, Prediction of workplace wet bulb global temperature, Applied occupational and environmental hygiene 14(2) (1999) 126-134.
[5] Z. Popp, I.S. Wing, K.J. Lane, G.A. Wellenius, A US heat disaster? Intersection of social vulnerability and temperature extremes exacerbated by mid-century climate change and population shifts, Environmental Research: Health 3(2) (2025) 025009.
[6] Q. Kong, R. Jing, C. Raymond, C. Tuholske, S. Heft-Neal, Z. Wagner, Z. Wang, A. Zimmer, M. Huber, E. Bendavid, Spatial patterns of historical changes in human heat stress disagree across metrics, Geophysical Research Letters 52(20) (2025) e2025GL117966.
[7] T. Chakraborty, Y. Qian, J. Li, L.R. Leung, C. Sarangi, Daytime urban heat stress in North America reduced by irrigation, Nature Geoscience 18(1) (2025) 57-64.
[8] A. Dajuma, M.B. Sylla, M. Tall, M. Almazroui, E. Afiesimama, A. Dosio, W. Moufouma-Okia, A. Diedhiou, F. Giorgi, Projected intensification and expansion of heat stress and related population exposure over Africa under future climates, Earth's Future 12(12) (2024) e2024EF004646.
[9] C.H. Simpson, O. Brousse, K.L. Ebi, C. Heaviside, Commonly used indices disagree about the effect of moisture on heat stress, NPJ climate and atmospheric science 6(1) (2023) 78.
[10] T. Chakraborty, Z.S. Venter, Y. Qian, X. Lee, Lower urban humidity moderates outdoor heat stress, Agu Advances 3(5) (2022) e2022AV000729.
[11] N. Freychet, G.C. Hegerl, N.S. Lord, Y.E. Lo, D. Mitchell, M. Collins, Robust increase in population exposure to heat stress with increasing global warming, Environmental Research Letters 17(6) (2022) 064049.
[12] C. McAllister, A. Stephens, S.M. Milrad, The heat is on: observations and trends of heat stress metrics during Florida summers, Journal of Applied Meteorology and Climatology 61(3) (2022) 277-296.
[13] C. Tuholske, K. Caylor, C. Funk, A. Verdin, S. Sweeney, K. Grace, P. Peterson, T. Evans, Global urban population exposure to extreme heat, Proceedings of the National Academy of Sciences 118(41) (2021) e2024792118.
[14] B.-J. He, J. Wang, H. Liu, G. Ulpiani, Localized synergies between heat waves and urban heat islands: Implications on human thermal comfort and urban heat management, Environmental Research 193 (2021) 110584.

[15] C. Wang, W. Zhan, Z. Liu, J. Li, L. Li, P. Fu, F. Huang, J. Lai, J. Chen, F. Hong, Satellite-based mapping of the Universal Thermal Climate Index over the Yangtze River Delta urban agglomeration, Journal of Cleaner Production 277 (2020) 123830.
[16] C. Jacobs, T. Singh, G. Gorti, U. Iftikhar, S. Saeed, A. Syed, F. Abbas, B. Ahmad, S. Bhadwal, C. Siderius, Patterns of outdoor exposure to heat in three South Asian cities, Science of the Total Environment 674 (2019) 264-278.
[17] K. Conlon, A. Monaghan, M. Hayden, O. Wilhelmi, Potential impacts of future warming and land use changes on intra-urban heat exposure in Houston, Texas, PloS one 11(2) (2016) e0148890.
[18] K.W. Oleson, A. Monaghan, O. Wilhelmi, M. Barlage, N. Brunsell, J. Feddema, L. Hu, D. Steinhoff, Interactions between urbanization, heat stress, and climate change, Climatic Change 129(3) (2015) 525-541.
[19] T. Zhang, Y. Zhou, K. Zhao, Z. Zhu, G. Chen, J. Hu, L. Wang, A global dataset of daily maximum and minimum near-surface air temperature at 1 km resolution over land (2003–2020), Earth Syst. Sci. Data, 14, 5637–5649, 2022.